

# Compensation temperature in spin-1/2 Ising trilayers: A Monte Carlo study

I. J. L. Diaz\* and N. S. Branco†

*Departamento de Física, Universidade Federal de Santa Catarina, 88040-900, Florianópolis, SC, Brazil*

(Dated: October 4, 2019)

We study the magnetic and thermodynamic properties of a spin-1/2 Ising system containing three layers, each of which is composed exclusively of one out of two possible types of atoms, **A** or **B**. The **A-A** and **B-B** bonds are ferromagnetic while the **A-B** bonds are antiferromagnetic. The study is performed through Monte Carlo simulations using the Wolff algorithm and the data are analyzed with the aid of the multiple-histogram reweighting technique and finite-size scaling tools. We verify the occurrence of a compensation phenomenon and obtain the compensation and critical temperatures of the model as functions of the Hamiltonian parameters. The influence of each parameter on the overall behavior of the system is discussed in detail and we present our results in the form of phase diagrams dividing the parameter space in regions where the compensation phenomenon is present or absent. Our results may provide invaluable information for experimentalists seeking to build materials with desired characteristics.

arXiv:1711.10367v3 [cond-mat.stat-mech] 2 Oct 2019

---

\* ianlopezdiaz@gmail.com

† nsbranco@gmail.com

## I. INTRODUCTION

The industry's commitment to producing ever-smaller electronic devices has contributed significantly to the increase in interest in the study of properties of thin films and other nanoscopic materials. From both theoretical and experimental points of view, there are many interesting behaviors and unusual phase diagrams that may arise when a magnet is composed of multiple layers with different magnetic properties. For instance, the existence of antiferromagnetic couplings between adjacent ferromagnetic layers generates a number of effects with great potential for important technological applications such as in magneto-optical recordings [1], spintronics [2], the giant magnetoresistance [3], and the magnetocaloric effects [4]. A particularly interesting phenomenon related to this type of layered ferrimagnets is the existence of compensation points, i.e., temperatures below the critical point for which the total magnetization is zero while the individual layers remain magnetically ordered [5]. The fact that the compensation point of some ferrimagnets occurs near room temperature makes them particularly important for applications in magneto-optical drives [1]. Interestingly, certain physical properties, such as coercivity, may exhibit a singular behavior at the compensation point, even though the compensation phenomenon is completely unrelated to criticality [1, 6, 7].

The development and improvement of thin film growth techniques, namely molecular-beam epitaxy (MBE) [8], metalorganic chemical vapor deposition (MOCVD) [9], pulsed laser deposition (PLD) [10, 11], and atomic layer deposition (ALD) [12, 13], have enabled the experimental realization of several layered materials with specific characteristics, such as bilayer [14], trilayer [15, 16], and multilayer [17–21] systems. Nevertheless, progress in experimental investigation of these materials becomes a slow and difficult process without detailed theoretical studies to guide. In this sense, several theoretical models (e. g, spin-1/2 Ising, spin-1 Ising, mixed-spin Ising, Potts, and Heisenberg models) have been used to advance the understanding of the properties of these magnetic systems.

Even the theoretical study of these systems has its difficulties, considering that only a handful of them are exactly solvable [22]; we must therefore resort to approximation methods. For instance, spin-1/2, spin-1 and mixed-spin Ising bilayers have been studied within various approaches, such as the mean-field approximation (MFA) [23–26], the effective-field approximation (EFA) [27–33], renormalization group (RG) [24, 34, 35], transfer matrix (TM) [23, 34, 36], high-temperature series expansion [26], and Monte Carlo (MC) simulations [24, 37–41]. A cellular automata (CA) simulation method was also employed in the analysis of both spin-1/2 Ising and 3-states Potts model bilayers [42]. The Green's function (GF) method was used to study a Heisenberg bilayer [43], and the pair approximation (PA) was also employed in the study of spin-1/2 Heisenberg and Ising bilayers [44, 45] and multilayers [46, 47]. Monte Carlo simulations were also applied in the study of Heisenberg [48] and Ising [49] multilayer systems.

On the other hand, trilayers and three-layered superlattices have not yet been studied as extensively as bilayers and multilayers. Among the few examples found in the literature, we mention an alternating spin-1/2, -1, and -3/2 Ising three-layered superlattice which was studied both in a mean-field approach [50] and through MC simulations [51]. We also cite a spin-1/2 Ising hexagonal lattice trilayer analyzed within the EFA [52] and a spin-1/2 Ising square lattice trilayer analyzed within both the MFA and the EFA [53].

In this work we are particularly interested in the type of system presented in Refs. 52 and 53, since these works show, in an effective-field approach, that it is possible for a single-spin system with an odd number of layers to exhibit a ferrimagnetic phase with compensation without site dilution, as opposed to the case of single-spin bilayers [41, 45] and multilayers [47, 49], for which dilution is a necessary condition for the existence of a non-zero compensation temperature. Therefore, we study a three-layer spin-1/2 Ising model with two types of atoms (**A** and **B**, say), such that each layer is composed of only one type of atom. Our goal is to establish the conditions for the appearance of the compensation effect and the contribution of each parameter to the occurrence of said effect. This model has already been analyzed in Ref. 53 within the MFA and EFA approaches, however, although mean-field-like approximations usually provide a fast and qualitatively right solution for most models, they do not always describe the actual physical behavior of some low-dimensional systems (see Ref. 54 and references therein). Therefore, we conduct this study within a Monte Carlo approach, using the Wolff single-cluster algorithm [55] and with the aid of a reweighting multiple histogram technique [56, 57] and finite-size scaling tools. In Sec. II we present the model and discuss the simulation and data analysis methods. We present our results and discussion in Sec. III. In Sec. IV, the final remarks and conclusions are drawn.

## II. MODEL AND MONTE CARLO SIMULATIONS

We study a trilayer system consisting of three monatomic layers,  $\ell_1$ ,  $\ell_2$ , and  $\ell_3$ , each of which is composed exclusively of either type-**A** or type-**B** atoms (see Fig. 1). The general system is described by the spin-1/2 Ising Hamiltonian

$$-\beta\mathcal{H} = K_{11} \sum_{\langle ii' \rangle} s_i s_{i'} + K_{22} \sum_{\langle jj' \rangle} s_j s_{j'} + K_{33} \sum_{\langle kk' \rangle} s_k s_{k'} + K_{12} \sum_{\langle ij \rangle} s_i s_j + K_{23} \sum_{\langle jk \rangle} s_j s_k, \quad (1)$$

where  $\langle ii' \rangle$ ,  $\langle jj' \rangle$ , and  $\langle kk' \rangle$  indicate summations over all pairs of nearest-neighbor sites in the same layer, whereas  $\langle ij \rangle$  and  $\langle jk \rangle$  are over pairs of nearest-neighbor sites in adjacent layers. The spin variables  $s_n$  assume the values  $\pm 1$ , the couplings are  $K_{\delta\eta} \equiv \beta J_{\delta\eta}$ , where  $\beta \equiv (k_B T)^{-1}$ ,  $T$  is the temperature,  $k_B$  is the Boltzmann constant, and the exchange integrals  $J_{\delta\eta}$  are  $J_{AA} > 0$  for **A-A** bonds,  $J_{BB} > 0$  for **B-B** bonds, and  $J_{AB} < 0$  for **A-B** bonds. We considered the two possible configurations of the trilayer in which there are more atoms of type-**A** than type-**B** (see Fig. 1), namely, the **AAB** system is the case in which  $J_{11} = J_{12} = J_{22} = J_{AA}$ ,  $J_{23} = J_{AB}$ , and  $J_{33} = J_{BB}$  (Fig. 1(a)), whereas the **ABA** system corresponds to  $J_{11} = J_{33} = J_{AA}$ ,  $J_{12} = J_{23} = J_{AB}$ , and  $J_{22} = J_{BB}$  (Fig. 1(b)).

For the Monte Carlo simulations, we employed the Wolff single-cluster algorithm [55] to analyze Hamiltonian (1) on a system of three stacked square lattices with  $L^2$  sites each. We used periodic boundary conditions on the  $xy$ -plane and free boundary conditions in the  $z$ -direction (see Fig. 1). The Metropolis [58] dynamics was also implemented in early stages of the work, but we preferred to use only the Wolff algorithm, considering that the single-spin flip dynamics proved extremely inefficient for high **A-B** coupling asymmetry. For both **AAB** and **ABA** trilayers, we performed simulations for linear sizes  $L$  from 10 to 100 and for a range of values of the Hamiltonian parameters:  $0.0 < J_{AA}/J_{BB} \leq 1.0$ , and  $-1.0 \leq J_{AB}/J_{BB} < 0.0$ . The Mersenne Twister pseudo-random number generator [59] was used to generate all random numbers throughout the simulations.

At every step of the simulation (i.e. every single-cluster update), we calculate the dimensionless energy  $\mathcal{E} \equiv \mathcal{H}/J_{BB}$ , the magnetizations in each layer

$$\mathcal{M}_\lambda = \frac{1}{L^2} \sum_{n \in \ell_\lambda} s_n, \quad (2)$$

where  $\lambda = 1, 2, 3$ , from which we obtain the total magnetization of the system, given by

$$\mathcal{M}_{\text{tot}} = \frac{1}{3}(\mathcal{M}_1 + \mathcal{M}_2 + \mathcal{M}_3). \quad (3)$$

The time series of  $\mathcal{E}$  and  $\mathcal{M}_\lambda$  were used to determine the relevant integrated autocorrelation time  $\tau$  after the initial  $t_{eq}$  steps were discarded to account for thermalization [60]. The number of steps performed in each simulation was always sufficient to generate at least  $10^4$  statistically independent states in order to calculate the canonical averages  $m_\Lambda \equiv \langle \mathcal{M}_\Lambda \rangle$ , where  $\Lambda = \text{tot}, 1, 2, 3$ . For instance, for the largest systems considered, i.e.,  $L = 100$ , we performed up to  $1.5 \times 10^6$  steps and obtained  $t_{eq} \approx 7.5 \times 10^4$  and  $\tau \approx 70$ . We also calculated the magnetic susceptibilities

$$\chi_\Lambda = N_\Lambda K (\langle \mathcal{M}_\Lambda^2 \rangle - \langle |\mathcal{M}_\Lambda| \rangle^2), \quad (4)$$

where  $N_1 = N_2 = N_3 = L^2$ ,  $N_{\text{tot}} = 3L^2$ , and  $K \equiv J_{BB}(k_B T)^{-1}$  is the inverse dimensionless temperature. The errors associated with the magnetizations and susceptibilities were determined through the jackknife method [60].

In Figs. 2 and 3, we show examples of the behavior of the magnetizations of the system as functions of temperature for the **AAB** and **ABA** trilayers, respectively. Both cases were obtained for  $J_{AA}/J_{BB} = 0.50$ . In Figs. 2(a), 2(b), 3(a), and 3(b), we show all magnetizations for  $L = 100$ , whereas in Figs. 2(c), 2(d), 3(c), and 3(d), we show only the total magnetization for several system sizes. In both **AAB** and **ABA** cases, for  $J_{AB}/J_{BB} = -0.1$  we see a compensation temperature  $T_{comp} < T_c$  such that  $m_{\text{tot}} = 0$  and  $m_1, m_2, m_3 \neq 0$  (Figs. 2(a), 2(c), 3(a), and 3(c)). For  $J_{AB}/J_{BB} = -1.0$ , on the other hand, we see no compensation effect (Figs. 2(b), 2(d), 3(b), and 3(d)).

For each set of values chosen for the parameters  $J_{AA}/J_{BB}$ ,  $J_{AB}/J_{BB}$ , and  $L$ , we performed simulations at several temperatures close to either the critical point or the compensation point. The data generated on the simulations were analyzed using the multiple-histogram method [56, 57] in order to obtain precise estimates for  $T_c$  and  $T_{comp}$  as functions of the Hamiltonian parameters. The methods used to determine the critical and compensations temperatures are discussed in Secs. III A and III B, respectively.

### III. RESULTS AND DISCUSSION

#### A. Determination of the critical temperatures $T_c$

In order to determine the critical point accurately, we employ a finite-size scaling analysis [61], in which we examine the size dependency of certain observables measured for finite systems of several sizes and extrapolate these results to the thermodynamic limit, i.e.,  $L \rightarrow \infty$ . In this approach, the singular part of the free energy density for a system of linear size  $L$ , near the critical point, is assumed to obey the following scaling form:

$$\bar{f}_{\text{sing}}(t, h, L) \sim L^{-d} f^0(tL^{yt}, hL^{yt}) \quad (5)$$

where  $d$  is the system dimensionality,  $t \equiv (T - T_c)/T_c$  is the reduced temperature,  $T_c$  is the critical temperature of the infinite system, and  $h$  is the external magnetic field given in units of  $k_B T$ . The RG dimensions associated with  $t$  and  $h$  are  $y_t = 1/\nu$  and  $y_h = (d + 2 - \eta)/2 = (\gamma + \beta)/\nu$ , respectively. The critical exponents  $\alpha$ ,  $\beta$ ,  $\gamma$  and  $\nu$  are the traditional ones associated, respectively, with the specific heat, magnetization, magnetic susceptibility, and correlation length.

We can use Eq. (5) to obtain the scaling forms for other thermodynamic quantities, e.g., for the magnetic susceptibilities at  $h = 0$ , it reads

$$\chi_\Lambda = L^{\gamma/\nu} \mathcal{X}_\Lambda(x_t), \quad (6)$$

where  $x_t \equiv tL^{1/\nu}$  is the temperature scaling variable.

As it is clear from the scaling law in Eq. (6), the susceptibilities diverge at the critical point only in the thermodynamic limit, whereas for a finite system size  $L$ , each  $\chi_\Lambda$  has a maximum at a pseudo-critical temperature  $T_c(L)$ , which asymptotically approaches the real  $T_c$  as  $L$  increases. This provides a powerful method to determine the critical point, since we know that the maximum occurs when

$$\left. \frac{d\mathcal{X}_\Lambda(x_t)}{dx_t} \right|_{T=T_c(L)} = 0, \quad (7)$$

we obtain the following relation

$$T_c(L) = T_c + aL^{-1/\nu}, \quad (8)$$

where  $a$  is a constant,  $T_c$  is the critical temperature and  $\nu$  is the critical exponent associated with the correlation length.

The finite-size scaling method is applicable to other quantities, such as the specific heat and other thermodynamic derivatives [62]. We expect the results obtained from the scaling behavior of these other quantities to be consistent, as we were able to verify in preliminary simulations. In this study, however, we focused only on the peak temperatures of the magnetic susceptibilities, defined in Eq. (4), for these peak temperatures occurred fairly close to one another and were the sharpest peaks from all the quantities initially considered.

To determine the pseudo-critical temperatures  $T_c(L)$ , we carry out simulations in a temperature range that contains the peaks of the susceptibilities. The range is typically divided in 8 to 15 equally spaced temperatures and we use the multiple-histogram method to obtain  $\chi_1$ ,  $\chi_2$ ,  $\chi_3$ , and  $\chi_{\text{tot}}$  as continuous functions of  $T$ , as shown in Fig. 4 for one of the susceptibilities ( $\chi_2$ ) of an **AAB** system with  $J_{AA}/J_{BB} = 0.8$ ,  $J_{AB}/J_{BB} = -0.5$ , and  $L$  from 10 to 100. The location of the peak temperatures is automated using the Broyden-Fletcher-Goldfarb-Shanno (BFGS) method [63, 64] and the errors are estimated using the blocking method [60], i.e., we divided the data from each simulation in blocks and repeated the procedure for each block. The errors are the standard deviation of the estimates obtained for different blocks.

The estimates of  $T_c(L)$  are then used as input in Eq. (8) to perform least-square fits. There are three free parameters in this equation to be adjusted in the fitting process, which is feasible but requires great statistical resolution in order to produce stable and reliable estimates for all the parameters involved. In the present work, however, we are interested only in the critical temperature and not in a precise value for the exponent  $\nu$ . Thus, to avoid an unnecessary increase in computational work, we employ the same procedure presented in Refs. 41, 49, and 65, in which we set a fixed value for the exponent  $\nu$  and perform fits with two free parameters, instead of three. These fits are made, for a fixed value of  $\nu$ , for system sizes not smaller than  $L_{\text{min}}$  and the value of  $L_{\text{min}}$  that gives the best fit is located, i.e., the one that minimizes the reduced weighted sum of errors,  $\chi^2/n_{DOF}$ , where  $n_{DOF}$  is the number of degrees of freedom. Next, we change the values of  $\nu$  and  $L_{\text{min}}$  iteratively until we locate the set of values that globally minimizes  $\chi^2/n_{DOF}$  and use these values to determine our best estimate of  $T_c$ .

In Fig. 5 we show examples of fits performed with Eq. (8) using the pseudo-critical temperatures obtained from the *maxima* of the magnetic susceptibilities for the case of an **AAB** trilayer with  $J_{AA}/J_{BB} = 0.80$  and  $J_{AB}/J_{BB} = -0.50$ . This fits were made using the values of  $L_{\text{min}}$  and  $\nu$  that minimize  $\chi^2/n_{DOF}$ . It is important to note that the statistical error obtained for  $T_c$  through this method is small, even negligible in some cases. Nonetheless, it is worth pointing out that this error is underestimated when compared to the value obtained through a true non-linear fit. Thus, to achieve a more realistic estimate for the error bar, we follow the criterion used in Refs. 41 and 49, in which the values obtained from fits that give  $\chi^2/n_{DOF}$  up to 20% larger than the minimum are considered in the statistical analysis.

Fig. 5 also shows that this procedure is not adequate for a precise determination of the values of  $\nu$ . Nonetheless, as it is not our goal to obtain a precise description of the critical behavior for the model, we use  $1/\nu$  only as an ‘‘effective exponent’’ in order to achieve a good estimate of  $T_c$ . Moreover, as discussed in Refs. 41 and 49, the final value of  $T_c$  obtained through this method is not sensitive to fluctuations around the value of  $\nu$  that minimizes  $\chi^2/n_{DOF}$ .

## B. Determination of the compensation temperatures $T_{comp}$

At the compensation temperature, we have  $m_{tot} = 0$  while  $m_1, m_2, m_3 \neq 0$ , as seen in Figs. 2(a), 2(b), 3(a), and 3(b). In order to estimate this temperature we perform simulations for a range of typically 5 to 8 equally spaced temperatures around  $T_{comp}$  and obtain the  $m_{tot}$  values as a continuous function of  $T$  using the multiple-histogram method, similarly to the procedure described in Sec. III A for  $T_c$ . In Fig. 6 we show the total magnetization as a function of temperature for the case of an **AAB** trilayer with  $J_{AA}/J_{BB} = 0.65$ ,  $J_{AB}/J_{BB} = -0.01$ , and several system sizes  $L$  from 20 to 100. In this figure, the solid lines were obtained using the multiple-histogram method. The procedure to determine the precise temperature where  $m_{tot}(T) = 0$  for each system size is also automated and we use Brent's method [66]. The error associated with  $T_{comp}$  is determined via the blocking method, as discussed in Sec. III A.

To obtain a final estimate of  $T_{comp}$ , it is necessary to combine the estimates for different system sizes. In Figs. 2(c) and 3(c) we see that different  $T_{comp}(L)$  are fairly close to one another. However, it is clear from Fig. 6 that the smaller lattices provide somewhat inconsistent results. Fig. 7 shows the size dependence of the compensation temperature estimates obtained from the same data depicted in Fig. 6. We can see that, as  $L$  increases, the compensation temperature approaches a fixed value. Thus, we fit our data to

$$T_{comp}(L) = a = \text{constant}, \quad (9)$$

for  $L \geq L_{min}$ , which corresponds to averaging the different compensation temperatures considering only the values of  $L$  after the  $T_{comp}(L)$  curve has approximately converged [41, 49]. The value of  $L_{min}$  is determined by minimizing the  $\chi^2/n_{DOF}$  of the fit. To estimate the final error bars we combine the error obtained in the fitting process with the largest error obtained for a fixed  $L$ . Note that Eq. (9) is consistent with the fact that the compensation phenomenon is not in any way related to criticality; thus, we have no *a priori* reason to expect a particular behavior (e.g., a power-law scaling form) for the dependence of  $T_{comp}$  on  $L$ .

## C. Phase diagrams

Our goal in this section is to outline the contribution of each parameter to the presence or absence of the compensation phenomenon. To that end we determine the regions of the parameter space for which the system has a compensation point, as seen in Figs. 2(a) and 2(c) for an **AAB** trilayer and Figs. 3(a) and 3(c) for an **ABA** system, and the regions for which the compensation effect does not take place, as seen in Figs. 2(b) and 2(d) for an **AAB** trilayer and Figs. 3(b) and 3(d) for an **ABA** system.

In order to analyze the influence of  $J_{AA}/J_{BB}$  in the behavior of the system, we fix a value for  $J_{AB}/J_{BB}$  and follow the procedures described in Sec. III A and Sec. III B to determine  $T_c$  and  $T_{comp}$  as functions of  $J_{AA}/J_{BB}$ , as seen in Fig. 8 for the **AAB** (Fig. 8(a)) and **ABA** (Fig. 8(b)) trilayers with  $J_{AB}/J_{BB} = -0.50$ . In both cases, the dotted vertical lines mark the value of  $J_{AA}/J_{BB}$  at which  $T_c = T_{comp}$  and above which there is no compensation for each system. Likewise, to understand the influence of  $J_{AB}/J_{BB}$  in the behavior of the trilayers, we fix a value for  $J_{AA}/J_{BB}$  and obtain  $T_c$  and  $T_{comp}$  as functions of  $J_{AB}/J_{BB}$ , as shown in Fig. 9 for both **AAB** (Fig. 9(a)) and **ABA** (Fig. 9(b)) trilayers with  $J_{AB}/J_{BB} = 0.50$ . The dotted vertical lines mark the value of  $J_{AB}/J_{BB}$  at which  $T_c = T_{comp}$  and below which there is no compensation for each system.

Our MC calculations can be compared to the EFA and MFA results reported in Ref. 53 for the same model. For instance, the qualitative behavior displayed in our Fig. 8(a) agrees with its MFA (Fig. 4(a) in Ref. 53) and EFA (Fig. 4(b) in Ref. 53) counterparts. The same is true for the comparison of our Fig. 8(b) with the analogous MFA (Fig. 5(a) in Ref. 53) and EFA (Fig. 5(b) in Ref. 53) ones. Nonetheless, the quantitative results are significantly different in all cases. Namely, in the same way the EFA values for the critical temperatures are consistently lower than those for the MFA [53], the same is true for the MC estimates, which are lower than both the EFA and MFA ones.

Comparing the  $T_c$  values in our Fig. 8(a) and those from Fig. 4 in Ref. 53, we can see that, for an **AAB** trilayer with  $J_{AB}/J_{BB} = -0.5$ , the EFA estimates range from 24.0% to 37.5% higher than the MC ones, whereas the MFA estimates are from 50.7% to 78.8% higher than the MC estimate. In both cases the largest discrepancy occurs for small  $J_{AA}/J_{BB}$  values. On the other hand, for  $T_{comp}$  this discrepancies are much smaller, being less than 1% in both the EFA and MFA for small  $J_{AA}/J_{BB}$  and increasing as  $T_{comp}$  approaches  $T_c$  at higher  $J_{AA}/J_{BB}$  values. For  $J_{AA}/J_{BB} = 0.5$  for example, the percentile deviation between the MFA and MC compensation temperatures is 18.0% while the EFA estimate is only 3.8% larger than its MC counterpart.

This is expected since both the mean-field and the effective-field approximations neglect spin-spin correlations that are fully taken into account in Monte Carlo simulations. Therefore, both MFA and EFA approaches overestimate the critical temperatures, whereas MC simulations provide  $T_c$  estimates that are much closer to the true values than their

mean-field-like counterparts. Since the effective-field approach still takes into account short-range correlations, which are entirely neglected by a standard MFA, the EFA temperatures should still be closer to the MC values than the MFA ones. It is worth stressing that the same occurs when we contrast pair approximation (PA) [45] and Monte Carlo [41] results for a site-diluted Ising bilayer, in which case the PA temperatures are higher than the MC ones. Although the PA takes into account longer-range correlations than both EFA and MFA, it still systematically overestimates the temperatures since it is a mean-field-like approximation. Thus, we would expect a PA study of the trilayer systems presented in this work to provide  $T_c$  estimates that are between the MC and EFA values for each set of Hamiltonian parameters.

Fig. 9 further helps to highlight the differences between MFA, EFA, and MC results. For  $J_{AA}/J_{BB} = 0.50$ , our MC simulations show that there is no compensation below  $J_{AB}/J_{BB} = -0.75 \pm 0.01$  and  $J_{AB}/J_{BB} = -0.532 \pm 0.002$  for the **AAB** and **ABA** trilayers, respectively. On the other hand, the mean-field and effective-field approximations predict that both types of trilayer will be in a ferrimagnetic phase with compensation for  $J_{AA}/J_{BB} = 0.50$ , irrespective of the value of  $J_{AB}/J_{BB}$ , as it is clear from Fig. 8 in Ref. 53.

Regarding the compensation temperature estimates obtained through different approximations, though, it is clear from the comparison between our Fig. 8 and Figs. 4 and 5 in Ref. 53, that there are no drastic differences between the MC, EFA, and MFA values. However, since the  $T_c$  estimates are systematically different for the approximations considered, as discussed in the last paragraph, we expect a significant change in the values of  $J_{AA}/J_{BB}$  for which the  $T_c$  and  $T_{comp}$  curves intersect, which we shall henceforth call  $(J_{AA}/J_{BB})^*$  for convenience. And in fact, for the **AAB** system, we have  $(J_{AA}/J_{BB})^* = 0.762381$ ,  $(J_{AA}/J_{BB})^* = 0.702061$ , and  $(J_{AA}/J_{BB})^* = 0.546 \pm 0.001$  for the MFA, EFA, and MC approaches, respectively. Similarly, for the **ABA** trilayer, we have  $(J_{AA}/J_{BB})^* = 0.875053$ ,  $(J_{AA}/J_{BB})^* = 0.796088$ , and  $(J_{AA}/J_{BB})^* = 0.526 \pm 0.001$  for the MFA, EFA, and MC approaches, respectively. This is a clear indication that the area of the region occupied by a ferrimagnetic phase with compensation is overestimated by the mean-field-like approximations, and that this area decreases as we increase the complexity of the approximation used.

If we repeat the procedure used to obtain Fig. 8 for other values of  $J_{AB}/J_{BB}$ , we can obtain a phase diagram dividing the parameter space of our Hamiltonian in two distinct regions of interest. One is a ferrimagnetic phase for which there is no compensation at any temperature and the second is a ferrimagnetic phase where there is a compensation point at a certain temperature  $T_{comp}$ . We present these results in Fig. 10 for the **AAB** trilayer. In this figure we also reproduce the MFA and EFA results reported in Ref. 53 for comparison purposes only. In all cases, the lines mark the separation between a ferrimagnetic phase with compensation (to the left) and a ferrimagnetic phase without compensation (to the right). Analogously, in Fig. 11 we present the MC, EFA, and MFA phase diagrams for the **ABA** system. These diagrams show that, in both trilayer types, there is always a compensation temperature for a sufficiently small  $J_{AA}/J_{BB}$  irrespective of the value of  $J_{AB}/J_{BB}$ , although the range of values of  $J_{AA}/J_{BB}$  for which the phenomenon occurs increases as the **A-B** interplanar coupling gets weaker. This behavior is consistent for MC, EFA, and MFA approaches and similar to what is reported for the diluted bilayer [41, 45] and multilayer [47, 49] systems for sufficiently small dilutions.

For the three approximations considered, the main difference we see when contrasting the behaviors depicted in Figs. 10 and 11 is that the lines separating the phases are closer to straight vertical lines for the **AAB** trilayer than for the **ABA** system, i.e., the value of  $(J_{AA}/J_{BB})^*$  is less sensitive to the value of  $J_{AB}/J_{BB}$  for the former system than for the latter. This is consistent with the fact that the number of **A-B** bonds in the **AAB** trilayer is only half that of the **ABA** system. In addition, Figs. 10 and 11 show that the area occupied by the ferrimagnetic phase with compensation in the  $J_{AB} \times J_{AA}$  diagrams is the smallest for the MC approach, followed by the EFA, and finally by the MFA. This happens for both types of trilayer and confirms the trend seen when comparing Fig. 8 with the results reported in Ref. 53. We see the same behavior when we contrast the PA [45] and MC [41] results for the Ising bilayer, in which case the smaller area is also obtained through Monte Carlo simulations, i.e., the area seems to decrease as we use more accurate approximations. Thus, we expect that if the pair approximation were applied to the trilayer systems, the line separating the phases with and without compensation would fall in between the dashed (EFA) and solid (MC) lines in both Figs. 10 (**AAB**) and 11 (**ABA**).

#### IV. CONCLUSION

In summary, we have investigated the magnetic and thermodynamic properties of a spin-1/2 Ising trilayer. The system is composed of three planes, each of which can only have atoms of one out of two types (**A** or **B**). The interactions between pairs of atoms of the same type (**A-A** or **B-B** bonds) are ferromagnetic while the interactions between pairs of atoms of different types (**A-B** bonds) are antiferromagnetic. The study is carried out in a Monte Carlo approach, aided by a multiple histogram reweighting technique and finite-size scaling methods. We verified the occurrence of a compensation phenomenon and determined the compensation temperatures, as well as the critical

temperatures of the model, for a range of values of the Hamiltonian parameters.

We present phase diagrams and a detailed discussion about the conditions for the occurrence of the compensation phenomenon. For instance, we see that the phenomenon is only possible if  $J_{AA} < J_{BB}$  and that the range of values of  $J_{AA}/J_{BB}$  for which there is compensation increases as  $|J_{AB}/J_{BB}|$  gets smaller, as it is also the case for similar systems containing a mixture of ferromagnetic and antiferromagnetic bonds [41, 45, 47]. The summary of the results is presented in a convenient way on  $J_{AB} \times J_{AA}$  diagrams which separate the Hamiltonian parameter-space in two distinct regions: one corresponding to a ferrimagnetic phase where the system has a compensation point and the other is a ferrimagnetic phase without compensation.

We compare our results with both mean-field and effective-field approximations applied to the same model [53] and we confirm that the compensation phenomenon is robust and occurs for all values of **A-B** exchanges in the range  $-1.0 \leq J_{AB}/J_{BB} < 0.0$ . Although it is clear from this comparison that the area of the parameter space occupied by the ferrimagnetic phase with compensation diminishes as we increase the accuracy of our approximation, the area obtained in this work through MC simulations is still fairly large if compared with the results for the diluted Ising bilayer [41] and multilayer [49] systems, especially as dilution is increased. It is worth stressing that our results show relevant quantitative differences with those obtained from MFA and EFA. Therefore, the MC results may be an important tool for experimentalists interested in building layered materials with a priori desired physical properties.

## ACKNOWLEDGMENTS

We are indebted to Prof. Dr. Lucas Nicolao for suggestions and helpful discussions. We would also like to thank Sigrid Anja Reichert for a critical reading of the manuscript. This work has been partially supported by the Brazilian Agency CNPq.

- 
- [1] G. Connell, R. Allen, and M. Mansuripur, *Journal of Applied Physics* **53**, 7759 (1982).
  - [2] P. Grünberg, R. Schreiber, Y. Pang, M. B. Brodsky, and H. Sowers, *Phys. Rev. Lett.* **57**, 2442 (1986).
  - [3] R. E. Camley and J. Barnaś, *Physical Review Letters* **63**, 664 (1989).
  - [4] M.-H. Phan and S.-C. Yu, *Journal of Magnetism and Magnetic Materials* **308**, 325 (2007).
  - [5] B. D. Cullity and C. D. Graham, *Introduction to magnetic materials*, 2nd ed. (John Wiley & Sons, New Jersey, USA, 2008).
  - [6] H.-P. D. Shieh and M. H. Kryder, *Applied physics letters* **49**, 473 (1986).
  - [7] J. Ostorero, M. Escorne, A. Pecheron-Guegan, F. Soulette, and H. Le Gall, *Journal of Applied Physics* **75**, 6103 (1994).
  - [8] M. A. Herman and H. Sitter, *Molecular beam epitaxy: fundamentals and current status*, Vol. 7 (Springer Science & Business Media, 2012).
  - [9] G. B. Stringfellow, *Organometallic vapor-phase epitaxy: theory and practice* (Academic Press, 1999).
  - [10] R. K. Singh and J. Narayan, *Phys. Rev. B* **41**, 8843 (1990).
  - [11] D. B. Chrisey and G. K. Hubler, (1994).
  - [12] M. Leskelä and M. Ritala, *Angewandte Chemie International Edition* **42**, 5548 (2003).
  - [13] S. M. George, *Chem. Rev* **110**, 111 (2010).
  - [14] M. Stier and W. Nolting, *Phys. Rev. B* **84**, 094417 (2011).
  - [15] C. Smits, A. Filip, H. Swagten, B. Koopmans, W. De Jonge, M. Chernyshova, L. Kowalczyk, K. Graszka, A. Szczerbakow, T. Story, *et al.*, *Physical Review B* **69**, 224410 (2004).
  - [16] J. Leiner, H. Lee, T. Yoo, S. Lee, B. Kirby, K. Tivakornsasithorn, X. Liu, J. Furdyna, and M. Dobrowolska, *Physical Review B* **82**, 195205 (2010).
  - [17] H. Kepa, J. Kutner-Pielaszek, J. Blinowski, A. Twardowski, C. F. Majkrzak, T. Story, P. Kacman, R. R. Gaazka, K. Ha, H. J. M. Swagten, W. J. M. de Jonge, A. Y. Sipatov, V. Volobuev, and T. M. Giebultowicz, *EPL (Europhysics Letters)* **56**, 54 (2001).
  - [18] G. Chern, L. Horng, W. K. Shieh, and T. C. Wu, *Phys. Rev. B* **63**, 094421 (2001).
  - [19] P. Sankowski and P. Kacman, *Phys. Rev. B* **71**, 201303 (2005).
  - [20] J.-H. Chung, Y.-S. Song, T. Yoo, S. J. Chung, S. Lee, B. Kirby, X. Liu, and J. Furdyna, *Journal of Applied Physics* **110**, 013912 (2011).
  - [21] T. Samburskaya, A. Y. Sipatov, V. Volobuev, P. Dziawa, W. Knoff, L. Kowalczyk, M. Szot, and T. Story, *Acta Physica Polonica A* **124**, 133 (2013).
  - [22] R. Baxter, *Exactly Solved Models in Statistical Mechanics*, Vol. 9 (Academic press London, London, UK, 1982).
  - [23] A. Lipowski and M. Suzuki, *Physica A: Statistical Mechanics and its Applications* **198**, 227 (1993).
  - [24] P. L. Hansen, J. Lemmich, J. H. Ipsen, and O. G. Mouritsen, *Journal of Statistical Physics* **73**, 723 (1993).
  - [25] T. Kaneyoshi, *Solid State Communications* **93**, 691 (1995).
  - [26] J. Oitmaa, *Phys. Rev. B* **72**, 224404 (2005).

- [27] T. Kaneyoshi and M. Jaščur, *Physica A: Statistical Mechanics and its Applications* **195**, 474 (1993).
- [28] M. Jaščur and T. Kaneyoshi, *Physica A: Statistical Mechanics and its Applications* **220**, 542 (1995).
- [29] A. Ainane, P. Häussler, K. Htoutou, and M. Saber, *Surface Science* **601**, 4256 (2007).
- [30] B. Deviren, O. Canko, and M. Keskin, *Journal of Magnetism and Magnetic Materials* **320**, 2291 (2008).
- [31] B. Deviren, S. Akbudak, and M. Keskin, *Solid State Communications* **151**, 193 (2011).
- [32] B. Deviren, Y. Polat, and M. Keskin, *Chinese Physics B* **20**, 060507 (2011).
- [33] E. Kantar and M. Erta, *Solid State Communications* **188**, 71 (2014).
- [34] Z. Li, Z. Shuai, Q. Wang, H. Luo, and L. Schülke, *Journal of Physics A: Mathematical and General* **34**, 6069 (2001).
- [35] B. Mirza and T. Mardani, *The European Physical Journal B-Condensed Matter and Complex Systems* **34**, 321 (2003).
- [36] A. Lipowski, *Physica A: Statistical Mechanics and its Applications* **250**, 373 (1998).
- [37] A. M. Ferrenberg and D. Landau, *Journal of applied physics* **70**, 6215 (1991).
- [38] A. Zaim, M. Kerouad, and M. Boughrara, *Solid State Communications* **158**, 76 (2013).
- [39] W. Wang, R. Liu, D. Lv, and X. Luo, *Superlattices and Microstructures* **98**, 458 (2016).
- [40] W. Wang, F.-l. Xue, and M.-z. Wang, *Physica B: Condensed Matter* **515**, 104 (2017).
- [41] I. J. L. Diaz and N. S. Branco, *Physica A: Statistical Mechanics and its Applications* **468**, 158 (2017).
- [42] Y. Asgari and M. Ghaemi, *Physica A: Statistical Mechanics and its Applications* **387**, 1937 (2008).
- [43] P. Xu and A. Du, *Physica B: Condensed Matter* **521**, 134 (2017).
- [44] K. Szałowski and T. Balcerzak, *Thin Solid Films* **534**, 546 (2013).
- [45] T. Balcerzak and K. Szałowski, *Physica A: Statistical Mechanics and its Applications* **395**, 183 (2014).
- [46] K. Szałowski and T. Balcerzak, *Physica A: Statistical Mechanics and its Applications* **391**, 2197 (2012).
- [47] K. Szałowski and T. Balcerzak, *Journal of Physics: Condensed Matter* **26**, 386003 (2014).
- [48] A. Razouk, M. Sahlaoui, and M. Sajjeddine, *Journal of superconductivity and novel magnetism* **24**, 1901 (2011).
- [49] I. J. L. Diaz and N. S. Branco, *Physica A: Statistical Mechanics and its Applications* **490**, 904 (2018).
- [50] S. Naji, A. Belhaj, H. Labrim, L. Bahmad, A. Benyoussef, and A. El Kenz, *Physica A: Statistical Mechanics and its Applications* **399**, 106 (2014).
- [51] S. Naji, A. Belhaj, H. Labrim, L. Bahmad, A. Benyoussef, and A. El Kenz, *Acta Phys Pol Ser B* **45**, 947 (2014).
- [52] J. P. Santos and F. S. Barreto, *Journal of Magnetism and Magnetic Materials* **439**, 114 (2017).
- [53] I. J. L. Diaz and N. S. Branco, *Physica B: Condensed Matter* **529**, 73 (2018), arXiv:1710.10298 [cond-mat].
- [54] B. Boechat, R. Filgueiras, C. Cordeiro, and N. Branco, *Physica A: Statistical Mechanics and its Applications* **304**, 429 (2002).
- [55] U. Wolff, *Phys. Rev. Lett.* **62**, 361 (1989).
- [56] A. M. Ferrenberg and R. H. Swendsen, *Phys. Rev. Lett.* **61**, 2635 (1988).
- [57] A. M. Ferrenberg and R. H. Swendsen, *Phys. Rev. Lett.* **63**, 1195 (1989).
- [58] N. Metropolis, A. Rosenbluth, M. Rosenbluth, A. Teller, and E. Teller, *J. Chem. Phys.* **21**, 1087 (1953).
- [59] M. Matsumoto and T. Nishimura, *ACM Transactions on Modeling and Computer Simulation (TOMACS)* **8**, 3 (1998).
- [60] M. E. J. Newman and G. T. Barkema, *Monte Carlo Methods in Statistical Physics* (Oxford University Press, New York, USA, 1999).
- [61] J. Yeomans, *Statistical Mechanics of Phase Transitions* (Clarendon Press, New York, USA, 1992).
- [62] A. M. Ferrenberg and D. P. Landau, *Phys. Rev. B* **44**, 5081 (1991).
- [63] C. G. Broyden, *IMA Journal of Applied Mathematics* **6**, 76 (1970).
- [64] C. G. Broyden, *IMA journal of applied mathematics* **6**, 222 (1970).
- [65] I. J. L. Diaz and N. S. Branco, *Physical Review E* **85**, 021142 (2012).
- [66] R. P. Brent, *SIAM Journal on Numerical Analysis* **10**, 327 (1973).

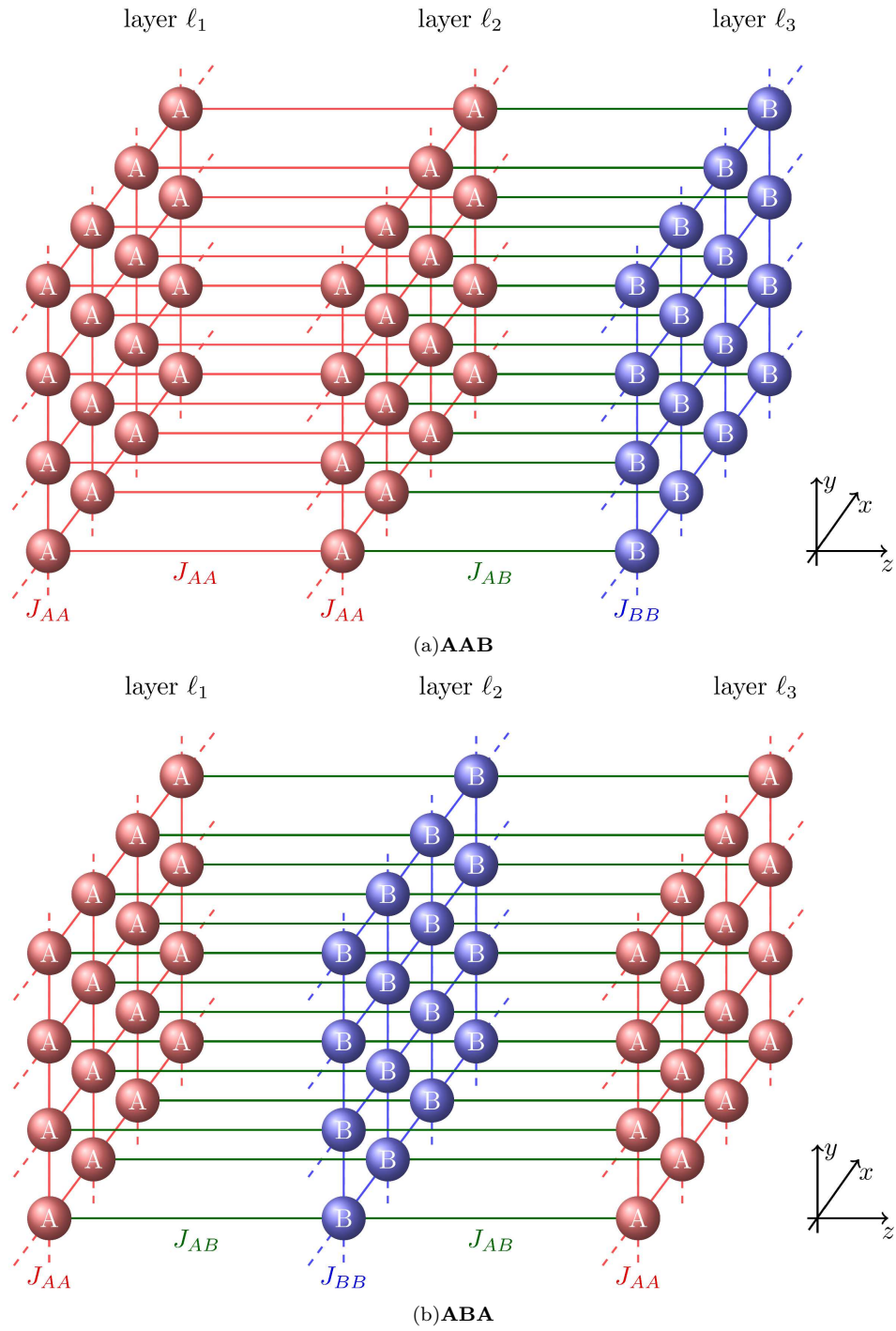


FIG. 1. A schematic representation of the trilayer systems. In (a), we have the **AAB** system, in which  $J_{11} = J_{12} = J_{22} = J_{AA} > 0$ ,  $J_{23} = J_{AB} < 0$ , and  $J_{33} = J_{BB} > 0$ . In (b), we have the **ABA** system, in which  $J_{11} = J_{33} = J_{AA} > 0$ ;  $J_{12} = J_{23} = J_{AB} < 0$ ;  $J_{22} = J_{BB} > 0$ .

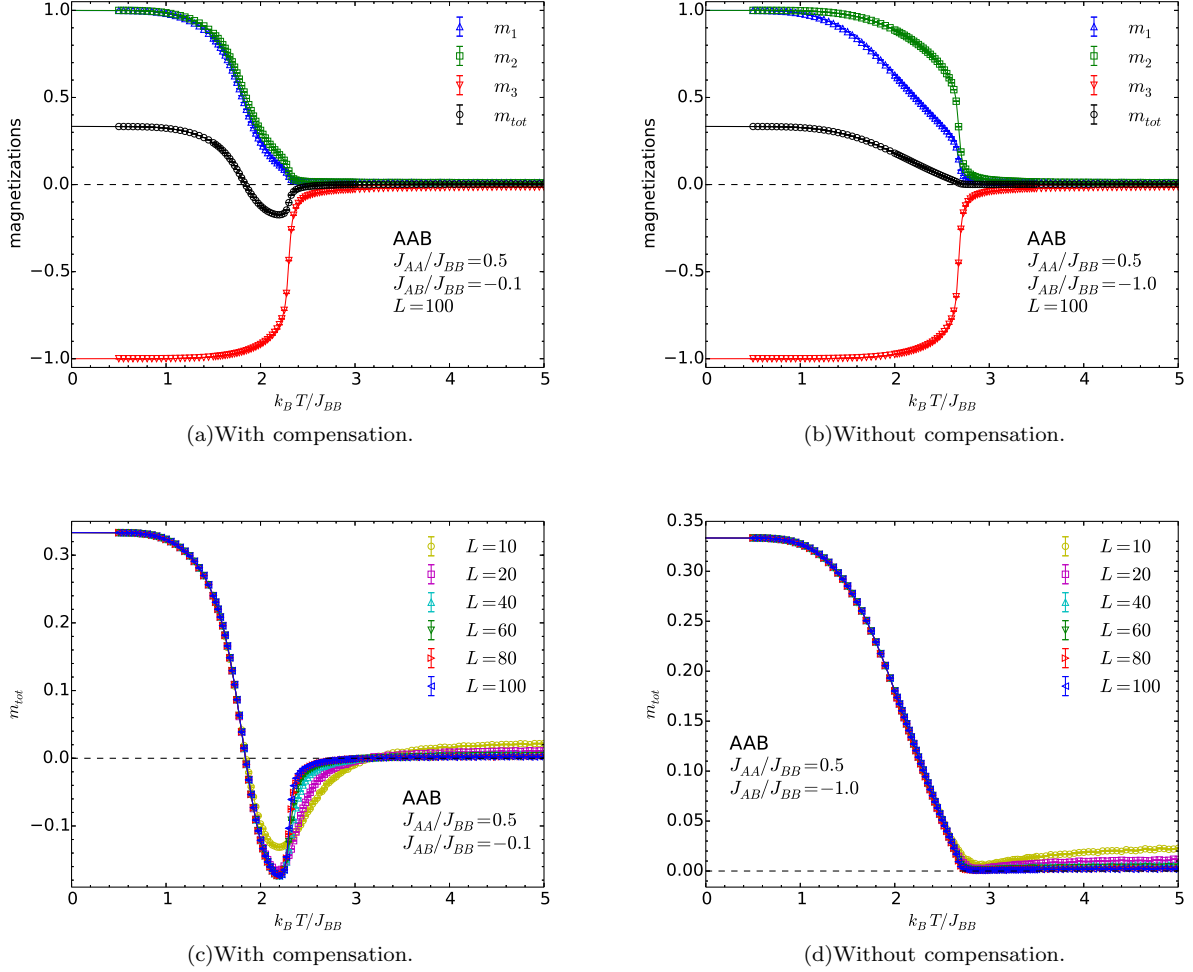


FIG. 2. Magnetizations as functions of the dimensionless temperature  $k_B T / J_{BB}$  for the **AAB** trilayer with  $J_{AA}/J_{BB} = 0.50$ . In (a) and (b) we show all magnetizations for  $L = 100$ , whereas for (c) and (d) we show only the total magnetization for several system sizes. Figures (a) and (c), for  $J_{AB}/J_{BB} = -0.1$ , show a compensation temperature  $T_{comp} < T_c$  such that  $m_{tot} = 0$ . Figures (b) and (d), for  $J_{AB}/J_{BB} = -1.0$ , show no compensation effect.

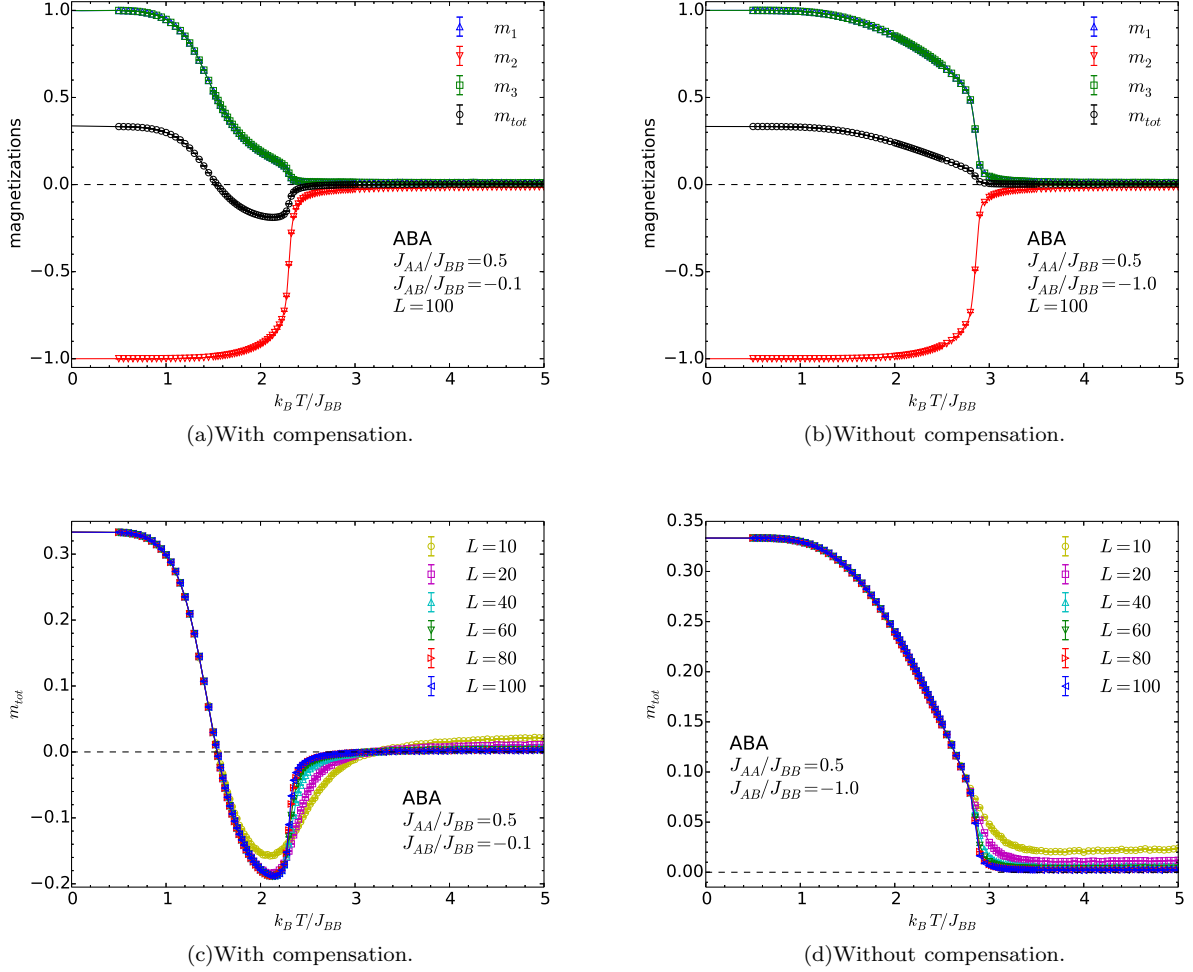


FIG. 3. (Color online) Magnetizations as functions of the dimensionless temperature  $k_B T / J_{BB}$  for the **ABA** trilayer with  $J_{AA}/J_{BB} = 0.50$ . In (a) and (b) we show all magnetizations for  $L = 100$ , whereas for (c) and (d) we show only the total magnetization for several system sizes. Figures (a) and (c), for  $J_{AB}/J_{BB} = -0.1$ , show a compensation temperature  $T_{comp} < T_c$  such that  $m_{tot} = 0$ . Figures (b) and (d), for  $J_{AB}/J_{BB} = -1.0$ , show no compensation effect.

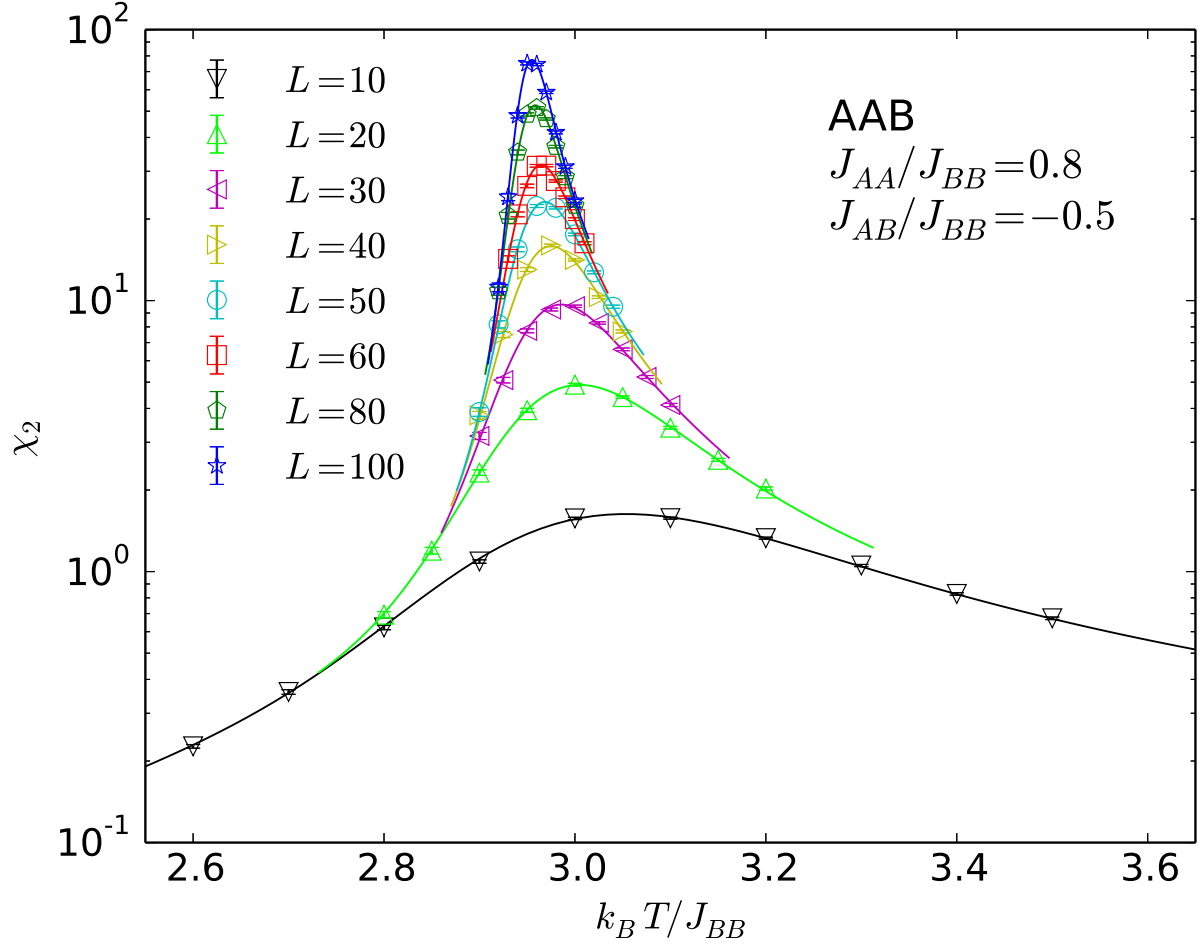


FIG. 4. Semilog plot of the magnetic susceptibility  $\chi_2$  as a function of the dimensionless temperature  $k_B T/J_{BB}$  for an **AAB** trilayer with  $J_{AA}/J_{BB} = 0.80$ ,  $J_{AB}/J_{BB} = -0.50$ , and linear lattice sizes  $L$  ranging from 10 to 100. The symbols correspond to simulation data and the solid lines were obtained using the multiple histogram method. Where the error bars are not visible, they are smaller than the symbols.

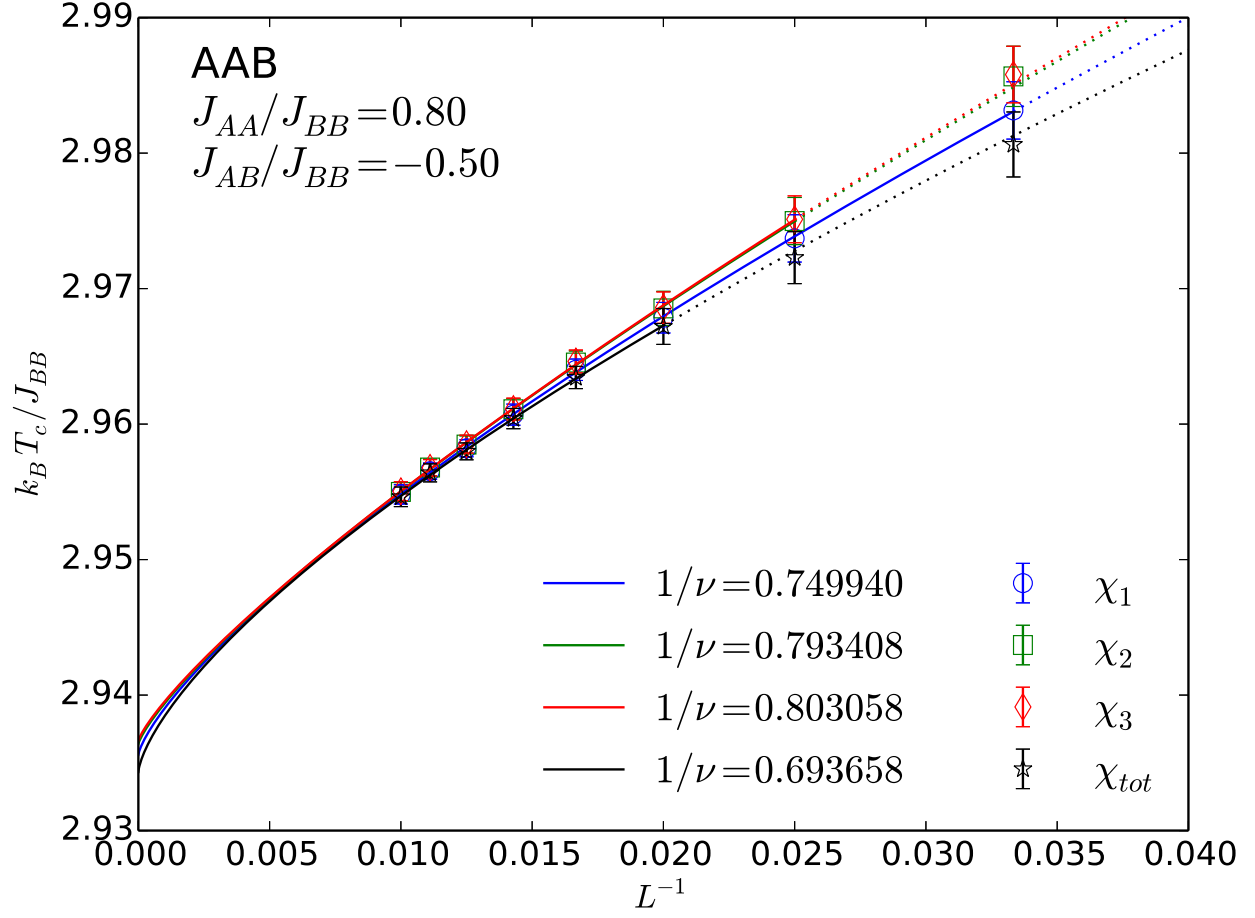


FIG. 5. Dimensionless effective critical temperature  $k_B T_c(L)/J_{BB}$  as a function of  $L^{-1}$  for an **AAB** trilayer with  $J_{AA}/J_{BB} = 0.80$  and  $J_{AB}/J_{BB} = -0.50$ . The symbols correspond to  $T_c(L)$  estimates made by locating the *maxima* of the magnetic susceptibilities  $\chi_1$  (circles),  $\chi_2$  (squares),  $\chi_3$  (diamonds), and  $\chi_{tot}$  (stars) for different system sizes. The solid lines are fits performed with Eq. (8) for  $L_{\min} \leq L \leq 100$  for the values of  $1/\nu$  which minimize the  $\chi^2/n_{DOF}$  for each case. The dotted lines are extrapolations of those fits for  $L < L_{\min}$ .

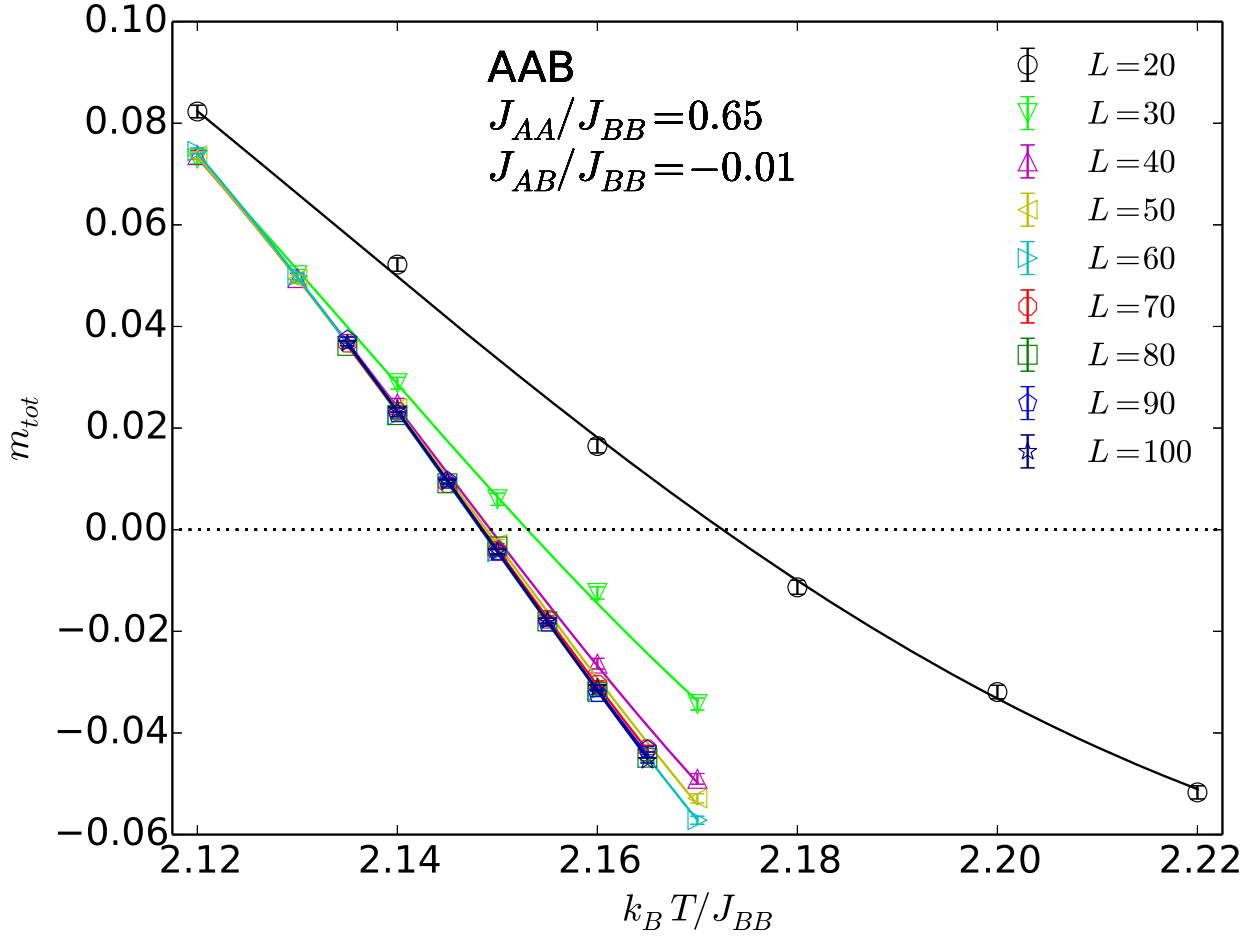


FIG. 6. Total magnetization as a function of the dimensionless temperature  $k_B T / J_{BB}$  for an **AAB** trilayer with  $J_{AA}/J_{BB} = 0.65$ ,  $J_{AB}/J_{BB} = -0.01$ , and linear lattice sizes  $L$  ranging from 20 to 100. The symbols correspond to simulation data and the solid lines were obtained using the multiple histogram method.

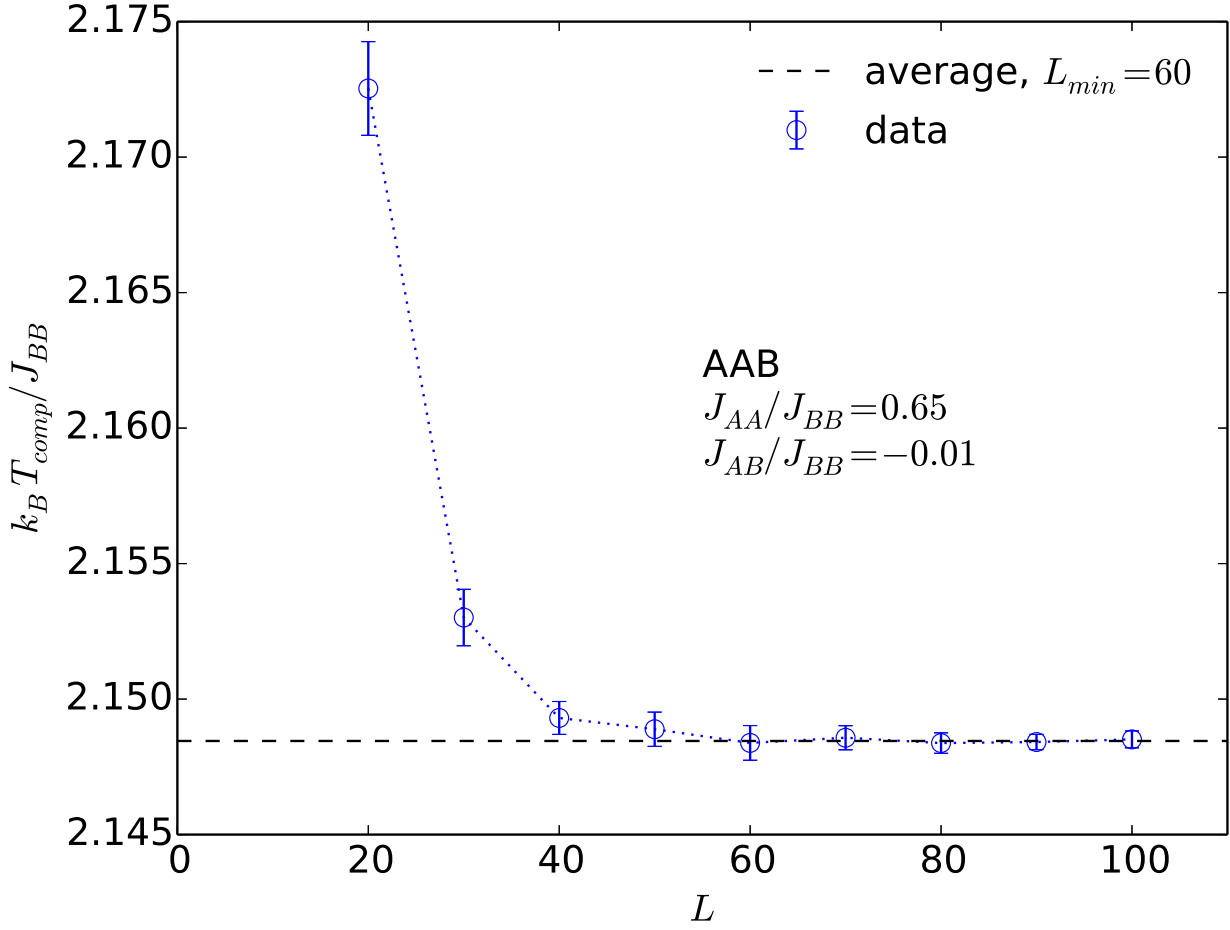


FIG. 7. Dimensionless compensation temperature  $k_B T_{comp}(L)/J_{BB}$  as a function of linear system size  $L$  for an **AAB** trilayer with  $J_{AA}/J_{BB} = 0.65$  and  $J_{AB}/J_{BB} = -0.01$ . The symbols are estimates made by locating the zero of the total magnetization for different system sizes. The dashed line is the average of the estimates obtained for  $L \geq 60$ , which is the value that minimizes the  $\chi^2/n_{DOF}$  of the fit in this particular case. The dotted lines are connecting the symbols just to guide the eye.

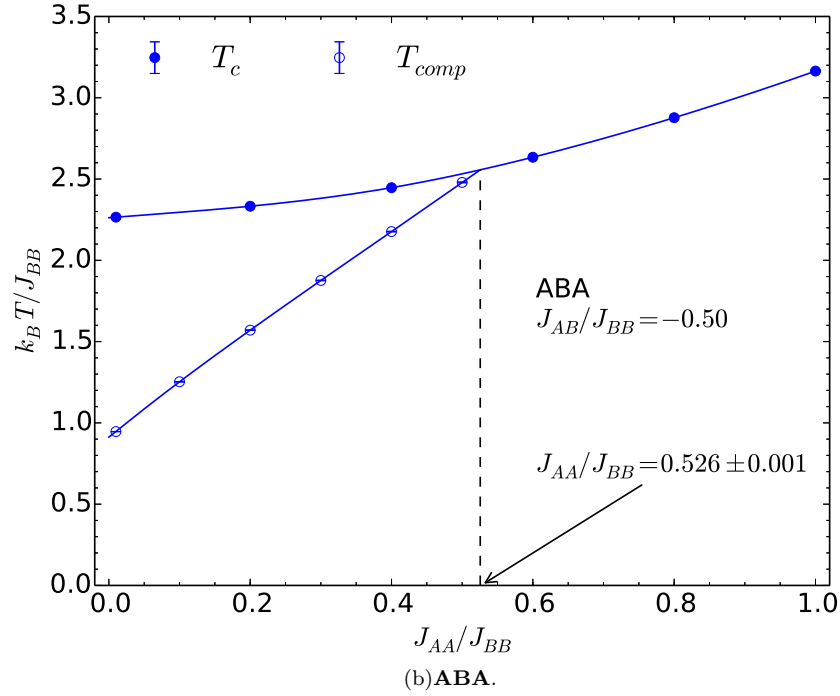
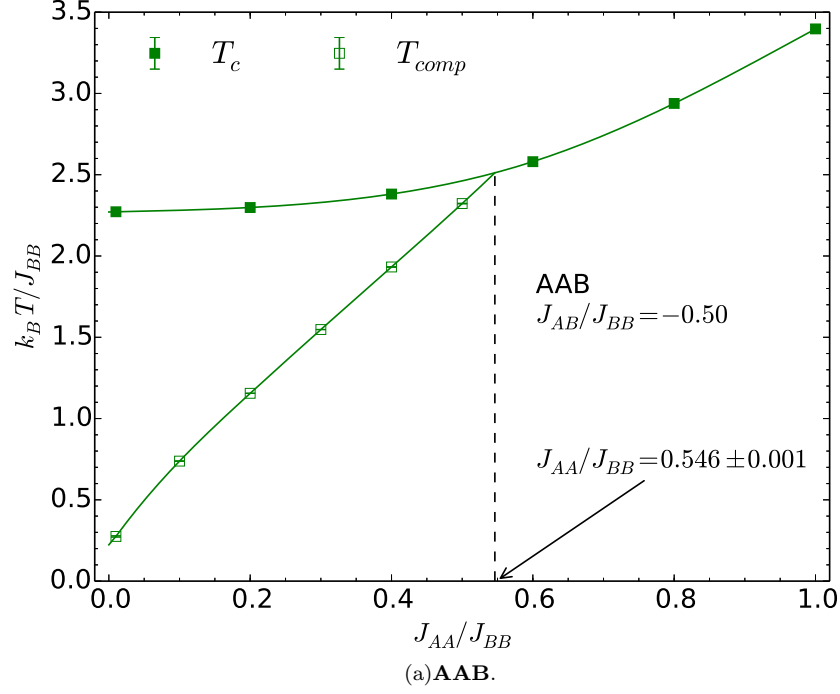


FIG. 8. Dimensionless critical temperature  $k_B T_c / J_{BB}$  (solid symbols) and compensation temperature  $k_B T_{comp} / J_{BB}$  (empty symbols) as functions of  $J_{AA} / J_{BB}$  for both (a) **AAB** and (b) **ABA** trilayers with  $J_{AB} / J_{BB} = -0.50$ . The dotted lines mark the values of  $J_{AA} / J_{BB}$  for which  $T_{comp} = T_c$  and above which there is no compensation.

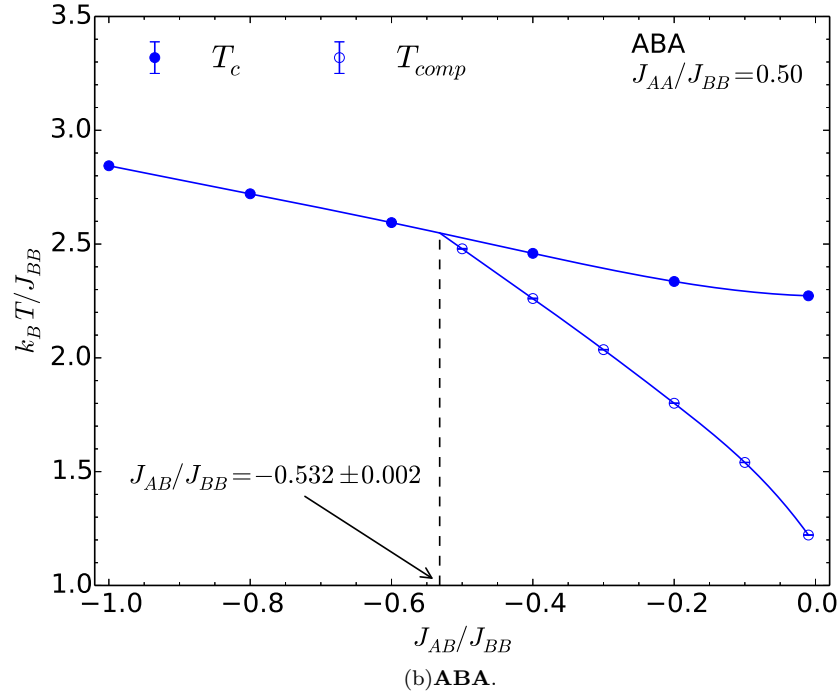
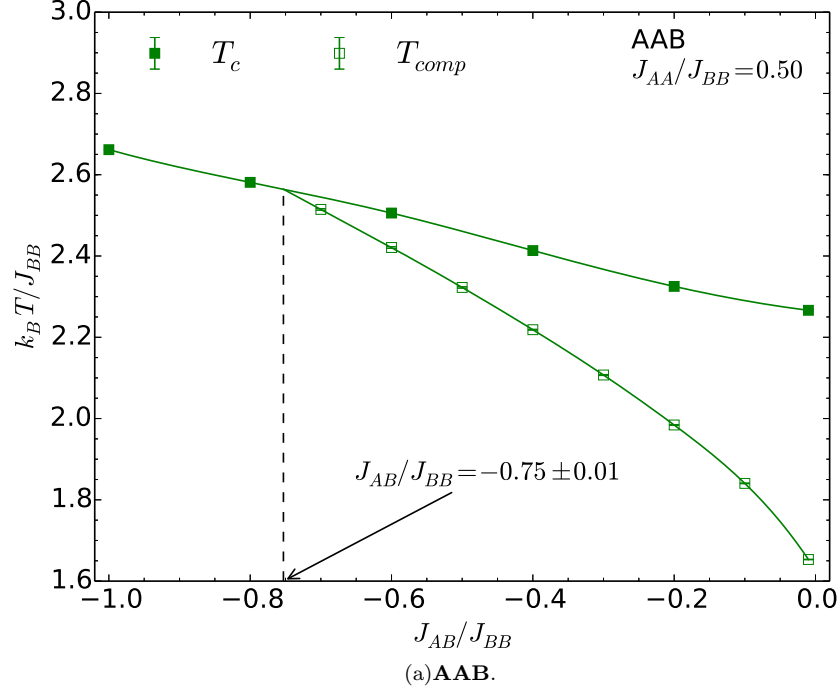


FIG. 9. Dimensionless critical temperature  $k_B T_c / J_{BB}$  (solid symbols) and compensation temperature  $k_B T_{comp} / J_{BB}$  (empty symbols) as functions of  $J_{AB} / J_{BB}$  for both (a) **AAB** and (b) **ABA** trilayers with  $J_{AA} / J_{BB} = 0.50$ . The dotted lines mark the values of  $J_{AB} / J_{BB}$  for which  $T_{comp} = T_c$  and below which there is no compensation.

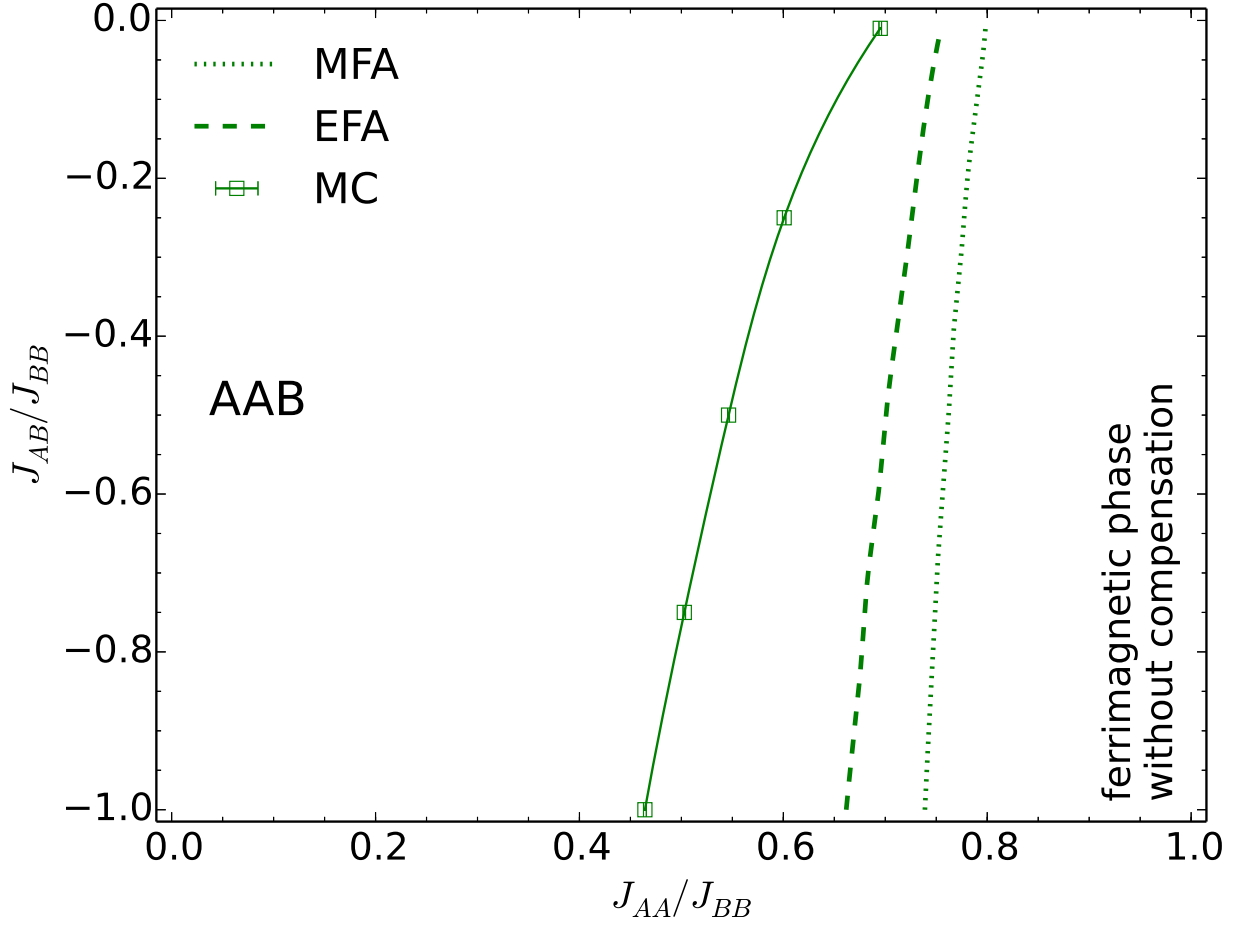


FIG. 10. Phase diagrams for the **AAB** trilayer. The squares were obtained through MC simulations and the solid lines are either cubic spline interpolations or linear extrapolations just to guide the eye. The effective-field approximation (dashed line) and mean-field approximation (dotted line) results correspond to those shown in Fig. 8 of Ref. 53 and are reproduced here for comparison purposes only. In all cases, the lines mark the separation between a ferrimagnetic phase with compensation (to the left) and a ferrimagnetic phase without compensation (to the right).

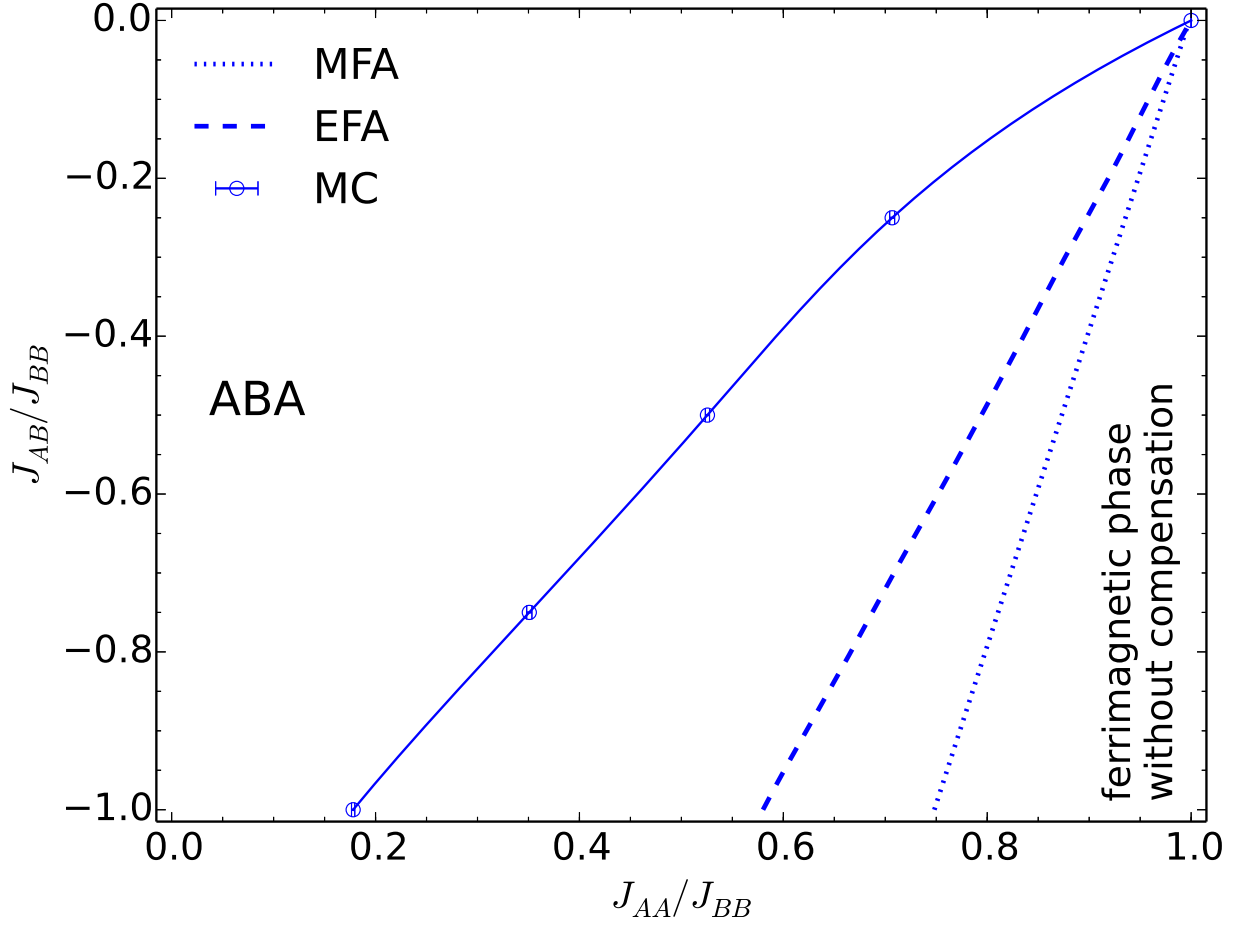


FIG. 11. Phase diagrams for the **ABA** trilayer. The circles were obtained through MC simulations and the solid lines are either cubic spline interpolations or linear extrapolations just to guide the eye. The effective-field approximation (dashed line) and mean-field approximation (dotted line) results correspond to those shown in Fig. 8 of Ref. 53 and are reproduced here for comparison purposes only. In all cases, the lines mark the separation between a ferrimagnetic phase with compensation (to the left) and a ferrimagnetic phase without compensation (to the right).